NWC TP 7121

Portable 45-Gigahertz Radar for Glint and Scintillation Studies

by
Robert J. Dinger
David R. Gagnon
David J. Banks
Erik W. van Bronkhorst
Research Department

DECEMBER 1990

NAVAL WEAPONS CENTER
CHINA LAKE, CA 93555-6001

Naval Weapons Center

FOREWORD

This report describes a 45-gigahertz (GHz) radar developed for the Glint and Scintillation Project during FY 88 and 89. This project, sponsored by the Naval Air Systems Command, ended in mid-FY 90; however, the radar has features useful in other measurement programs. This report has been written to disseminate information about the radar's capabilities to program offices and other potential sponsors. In addition, designers of radar cross-section measurement radars may find several of the features implemented in the 45-GHz radar of interest, and this report is directed at them as well.

Discussions with numerous colleagues at the Naval Weapons Center were beneficial during the development of this radar, but special thanks are appropriate for R. Skatvold and M. Sanders.

This report was reviewed for technical accuracy by Michael Mumford.

Approved by
R. L. DERR, *Head*
Research Department
21 December 1990

Under authority of
D. W. COOK
Capt., U.S. Navy
Commander

Released for publication by
W. B. PORTER
Technical Director

NWC Technical Publication 7121

Published by ..... Technical Information Department
Collation ..... Cover, 14 leaves
First printing ..... 95 copies

REPORT DOCUMENTATION PAGE

Form Approved
OMB No. 0704-0188

1. AGENCY USE ONLY (*Leave blank*)	2. REPORT DATE	3. REPORT TYPE AND DATES COVERED
	Dec 90	Final, 88 Oct to 90 Sep

4. TITLE AND SUBTITLE
PORTABLE 45-GIGAHERTZ RADAR FOR GLINT AND SCINTILLATION STUDIES

5. FUNDING NUMBERS
PE 64258N
WU W0610

6. AUTHOR(S)
R. J. Dinger, D. R. Gagnon, D. J. Banks, and
E. W. van Bronkhorst

7. PERFORMING ORGANIZATION NAME(S) AND ADDRESS(ES)
Naval Weapons Center
China Lake, CA 93555-6001

8. PERFORMING ORGANIZATION REPORT NUMBER
NWC TP 7121

9. SPONSORING/MONITORING AGENCY NAME(S) AND ADDRESS(ES)
Naval Air Systems Command
Washington, DC 20361

10. SPONSORING/MONITORING AGENCY REPORT NUMBER

11. SUPPLEMENTARY NOTES

12a. DISTRIBUTION/AVAILABILITY STATEMENT
A Statement; public release; unlimited distribution

12b. DISTRIBUTION CODE

13. ABSTRACT (*Maximum 200 words*)

(U) A 45-gigahertz radar has been developed that yields full-polarization inverse synthetic aperture radar images and instantaneous angle-of-arrival measurements for angular scintillation studies. The system is portable, self-contained, and suitable for measurements on radar cross-section ranges and open, unprepared sites. Measurements have been made successfully on large scale-model targets (8 meters in extent) at ranges up to 1000 meters.

14. SUBJECT TERMS
Glint
Angular Scintillation
Millimeter-Wave Radar
ISAR Imaging
Radar Cross-Section Measurements

15. NUMBER OF PAGES
26

16. PRICE CODE

17. SECURITY CLASSIFICATION OF REPORT	18. SECURITY CLASSIFICATION OF THIS PAGE	19. SECURITY CLASSIFICATION OF ABSTRACT	20. LIMITATION OF ABSTRACT
UNCLASSIFIED	UNCLASSIFIED	UNCLASSIFIED	UL

CONTENTS

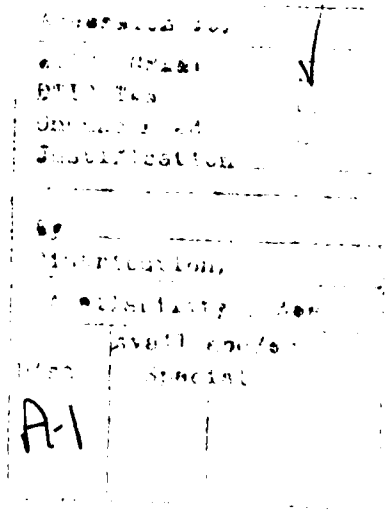

1. INTRODUCTION

Angular scintillation (glint) in the tracking loop of a radio frequency (RF) missile seeker arises from warps in the phase front of the scattered wave produced by interference between the individual centers of scattering on a complex target. Because the seeker attempts to orient itself at right angles to the phase front, these warps can produce a substantial displacement between the apparent radar center and the physical center of the target.

Glint is one the major limiting factors in terminal guidance accuracy for an RF-guided missile. Given this circumstance, the evaluation of missile seekers in hardware-in-the-loop (HWIL) test chambers clearly must use target models that reproduce accurately the glint characteristics of a given target in all regards, such as proper size and aspect angle dependence, complete polarization dependence, and proper correlation between radar cross section (RCS) and glint. The Naval Weapons Center is currently gathering measurements on a variety of scale-model and full-size targets for the purpose of developing glint and RCS models for HWIL chambers.

This report describes a 45-gigahertz (GHz) fully polarimetric imaging radar that was developed for these measurements. The 45-GHz frequency was chosen to give a full-size-equivalent frequency of about 9 GHz for the one-fifth-scale targets measured with the radar. As with a number of instrumentation radars in recent years, we designed the system around a Hewlett-Packard (HP) 8510B network analyzer. Three features of this radar distinguish it from other existing inverse synthetic aperture radars (ISARs):

- Since the largest targets have a size L of approximately 8 meters, the size-to-wavelength ratio is $L/\lambda = 1200$. This ratio is significantly larger than most ISAR installations and requires that special consideration be given to the possibility of image blurring by spurious target and pylon motion.

- The measurements are taken on an outdoor RCS facility at a range of 1000 meters. Most millimeter-wave ISAR facilities use indoor anechoic chambers. This large range requires a delay line in the reference arm of the HP-8510B.

- For comparison with the apparent radar center of scattering calculated from the ISAR-image-derived models, an independent monopulse processing channel was implemented in the radar. The monopulse output provides continuous "ground truth" measurement of the center of scattering by measuring the angle of arrival (AOA).

Although the radar was developed for a specific purpose (Glint and Scintillation Project), it also has application to general-purpose RCS and ISAR measurements. The entire system is portable and intended for out-of-door applications.

Below, we first review briefly the fundamentals of ISAR imaging, emphasizing that the image can be thought of as a scattering center "map" of the target. From this map, with suitable approximations, we then show that the RCS and the apparent AOA (glint) can be calculated. We then present the details of the radar. We elaborate on several special problems encountered for this measurement, including the need for the shortest possible measurement time and concerns about spurious motion of the target. Calibration of the radar is then discussed. We close with examples of ISAR images and other data taken with the radar.

2. ISAR IMAGING AND TARGET SCATTERING MODELS

2.1. ISAR IMAGING FUNDAMENTALS

Referring to Figure 1, ISAR imaging seeks to recover the target reflectivity distribution g(x,y) in the x-y plane by measuring the RCS coherently as the target

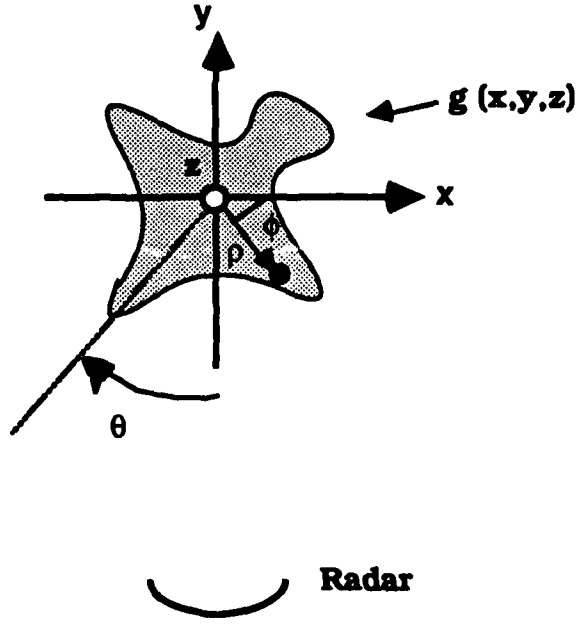

FIGURE 1. Target With Reflectivity Distribution g(x,y,z) Rotating on Pylon in the x-y Plane. A typical scattering center at (ρ,ϕ) is highlighted.

is rotated through an angle θ. Taking the body-fixed coordinates of a general point on the target as ρ and ψ, this point produces a phase variation at the radar receiver given by

$$\eta(f,\theta) = \exp [j4\pi f\rho \cos (\theta - \psi)/c] \ , \tag{1}$$

where f is the frequency. Expanding the cosine and defining $f_y = -2f \cos \theta/c$ and $f_x = 2f \sin \theta/c$, the phase variation can be written as

$$\eta(f_x, f_y) = \exp [j\ 2\pi (f_x x + f_y y) \ . \tag{2}$$

At any given θ and f, the *total* measured signal is given by

$$\sigma(f_x, f_y) = \iint g(x,y) \exp [j\ 2\pi (f_x x + f_y y)] \, dx \, dy \ . \tag{3}$$

Taking the inverse two-dimensional Fourier transform of Equation 3 then yields the desired result:

$$g(x,y) = \iint h(f_x, f_y)\, \sigma(f_x, f_y) \exp [-j\ 2\pi (f_x x + f_y y)] \, df_x \, df_y \ , \tag{4}$$

where $h(f_x, f_y)$ is the windowing function.

From the properties of the Fourier transform, the downrange resolution Δy is related to the bandwidth B by

$$\Delta y = ck/2B \ , \tag{5}$$

where k is a constant of order unity that depends on the specific $h(f_x, f_y)$. For a rectangular window, k = 1.0. The cross-range resolution Δx is related to the extent of the aspect angle window (i.e., the angular change over which a single image is formed) Δθ by

$$\Delta x = c/2f_0 \, \Delta\theta \ , \tag{6}$$

where f_0 is the lower edge of the band over which the radar is swept.

2.2. TARGET SCATTERING MODEL CONSTRUCTION

Each target reflectivity distribution g(x,y) constitutes a "radar image" of the target in the plane normal to the axis of rotation. In fact, of course, g(x,y) changes as the target is rotated: New scatterers come into view, other scatterers are shadowed, the scatterers are nonisotropic, and specular scattering produces a scattering center that is not fixed on the target. In addition, the reflectivity distribution is polarization dependent. Hence, the reflectivity distribution should be annotated as $g_{tr,\theta o}(x,y)$, where t and r refer to the transmit and receive polarization states, and θ_0 is the aspect angle of the center of the angular window.

For the construction of scattering center maps, *three*-dimensional images are desirable (i.e., reflectivity distributions given by $g_{tr,(\theta o,\phi o)}(x,y,z)$, where θ_0 and ϕ_0 denote

the polar angles of the radar line-of-sight relative to the target). However, rotating the model targets on a pylon about any arbitrary axis is difficult; hence, full solid angle coverage for $g_{tr,(\theta o,\phi o)}(x,y,z)$ is not possible. Given the available subset of possible images $g_{tr,(\theta o,\phi o)}(x,y,z)$, the model construction process consists of locating the major scatterers and then using the polarization properties and angular dependence as revealed in the images to identify and categorize them.

The end result is a scattering center *map* of the target from which various target properties of interest (RCS and glint) can be simulated in a HWIL chamber. Or, the scattering center maps can be analyzed for application to target-modeling and target-identification purposes. The map is a set of scattering strengths and phases $(A_j \, , \phi_j)_{tr}$ located at positions r_j, where r_j is a position vector defined with respect to a coordinate system fixed within the target. The *tr* subscript is attached to indicate that the $(A_j \, , \phi_j)$ depend on the transmit and receive polarizations. Implicit in this approach to target modeling are two assumptions: (1) The wavelength is much less than both the target overall size and the size of any structures on the target and (2) multiple-bounce scattering between scattering centers is negligible.

2.3. CALCULATION OF GLINT AND RCS FROM A SCATTERING CENTER MAP

From a scattering center map (A_j, ϕ_j, r_j), the apparent AOA can be calculated by the following equation (Reference 1):

$$\eta = \frac{\Sigma_j \Sigma_i A_j A_i \alpha_j \cos(\beta_j - \beta_i)}{\Sigma_j \Sigma_i A_j A_i \cos(\beta_j - \beta_i)} \, , \tag{7}$$

where $\alpha_j = 2k\mathbf{a} \cdot \mathbf{r}_j/R$, $\beta_j = 2k\mathbf{R} \cdot \mathbf{r}_j + \phi_j$, $\mathbf{R}$ is a unit vector directed from the radar to the target, R is the range from the radar to the target, $k = 2\pi/\lambda$, and the sums are taken from 1 to the number of scattering centers N. η is the AOA measured from the direction of R, and $\mathbf{a}$ is a unit vector orthogonal to R. We have suppressed the polarization dependence in this simplified version of the glint equation. Similarly, the RCS is given by

$$\sigma = |\Sigma_i A_i \exp(j2k\mathbf{R} \cdot \mathbf{r}_i)|^2 \, . \tag{8}$$

We would like to have confidence that the angle calculated from the scattering center maps by Equation 7 agrees with the angle that would actually be measured by a tracking radar. To develop this confidence, a monopulse antenna and receiver were implemented in the radar, in addition to the ISAR receiver.

3. DESCRIPTION OF RADAR

3.1. OVERVIEW

The radar was designed to operate on a far-field RCS facility at a radar-to-target range of 1000 meters (Figure 2). Figures 3 and 4, respectively, are external and interval views of the radar van and antenna assembly. The van and antenna mounting assembly are portable, permitting measurements as needed in a variety of locations. The antenna gimbal in Figure 3 permits fine scanning (needed for the monopulse receiver calibration) and alignment of the antennas over a ±10-degree angular region.

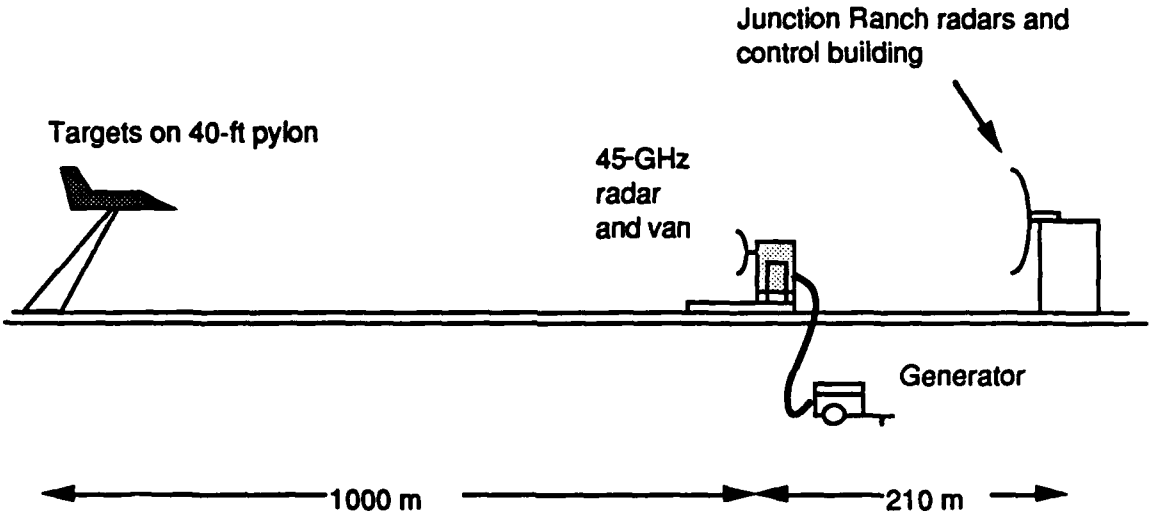

FIGURE 2. Radar Configuration at Junction Ranch RCS Range.

Table 1 summarizes the capabilities of the radar, and Figure 5 is an overall block diagram. The radar has three major sections: transmitter; RCS/ISAR receiver; and monopulse receiver. Figure 6 is a block diagram of the transmit and RCS/ISAR sections, and Figure 7 is a block diagram of the monopulse section.

The 44- to 46-GHz radar signal is generated by mixing a 5- to 7-GHz signal (derived from a synthesizer) with a 39-GHz local oscillator signal. Typically, 201 frequency points are used over a 2-GHz bandwidth. This combination produces an alias-free range of only 30 meters, so that a target at a range of 1000 meters would be masked by clutter foldover, even in the fully phase-locked stepped-frequency mode of the HP-8510B. To shift the reference plane to the target zone, a 6.5-microsecond (μs) delay line is inserted in the reference channel path; this approach also allows us to use the much higher data rate of the HP-8510B ramp mode. Because a 6.5-μs delay line was not available with sufficient bandwidth at 5 to 7 GHz, the synthesizer is swept from 1.25 to 1.75 GHz and the delay provided in this band; frequency quadruplers then recover the 5- to 7-GHz signals needed. The HP-8510B is operated in the multisource mode with a factor-of-four frequency offset for proper frequency registration of synthesized and detected signals.

As described below, this reference plane-shift is also needed to ensure that the detected signal does not fall outside of the final 10-kilohertz (kHz) bandwidth of the HP-8510B detector.

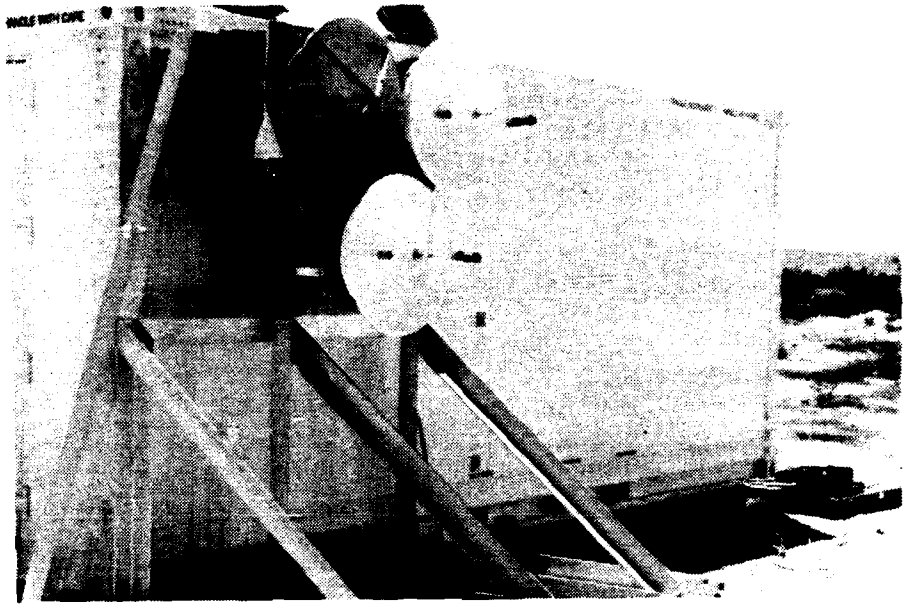

FIGURE 3. Outside View of the Radar Van and Antennas.

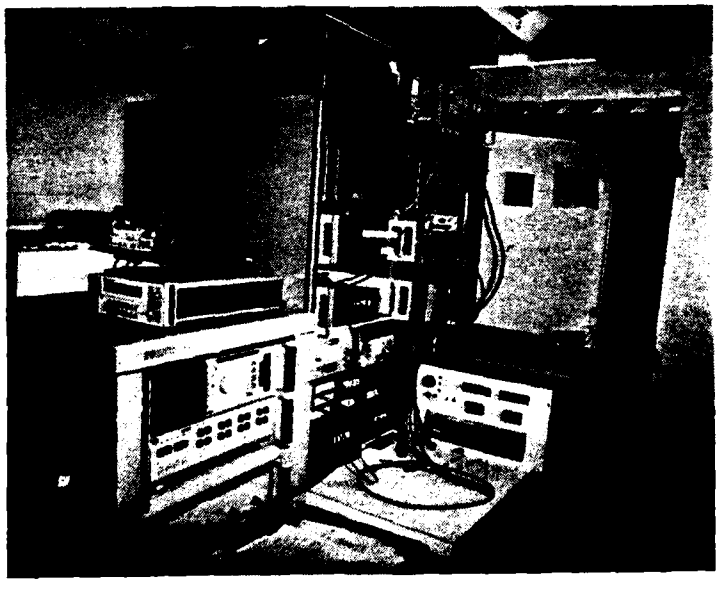

FIGURE 4. Interior View of the Radar Van.

TABLE 1. Radar Parameters

Parameter	Value
Center frequency	45 GHz
Bandwidth	2.0 GHz
Modulation format	Swept frequency, continuous wave (CW)
Number of frequencies	201 or 401
Time for one complete 4-polarization range cut	0.76 second
Time for 2-polarization range cut	0.38 second
Target range	1000 meters
Transmitter	
Amplifier type	TWT
Output power	30.0 watts, average
Polarization states	Linear vertical and horizontal
Antenna diameter	60 centimeters
Antenna gain	47 decibels
Beamwidth	0.5 degree
Polarization isolation	Greater than 20 decibels
Imaging receive channel	
First intermediate freq (IF)	5 to 7 GHz
Second IF	10 MHz
Final bandwidth	10 kHz
Antenna diameter	60 centimeters
Antenna gain	47 decibels
Beamwidth	0.5 degree
Polarization isolation	Greater than 20 decibels
Monopulse receive channel	
Antenna diameter	60 centimeters
Feed type	TE_{10} waveguide, four ports
Feed polarization	Vertical
Sum beam gain	47 decibels
Beamwidth	0.5 deg
Difference null depth	At least 30 decibels

Orthomode transducers in both the transmitter and the receiver channels separate the horizontal and vertical polarizations. The transmit power amplifier is a 30-watt high gain traveling-wave-tube (TWT) amplifier.

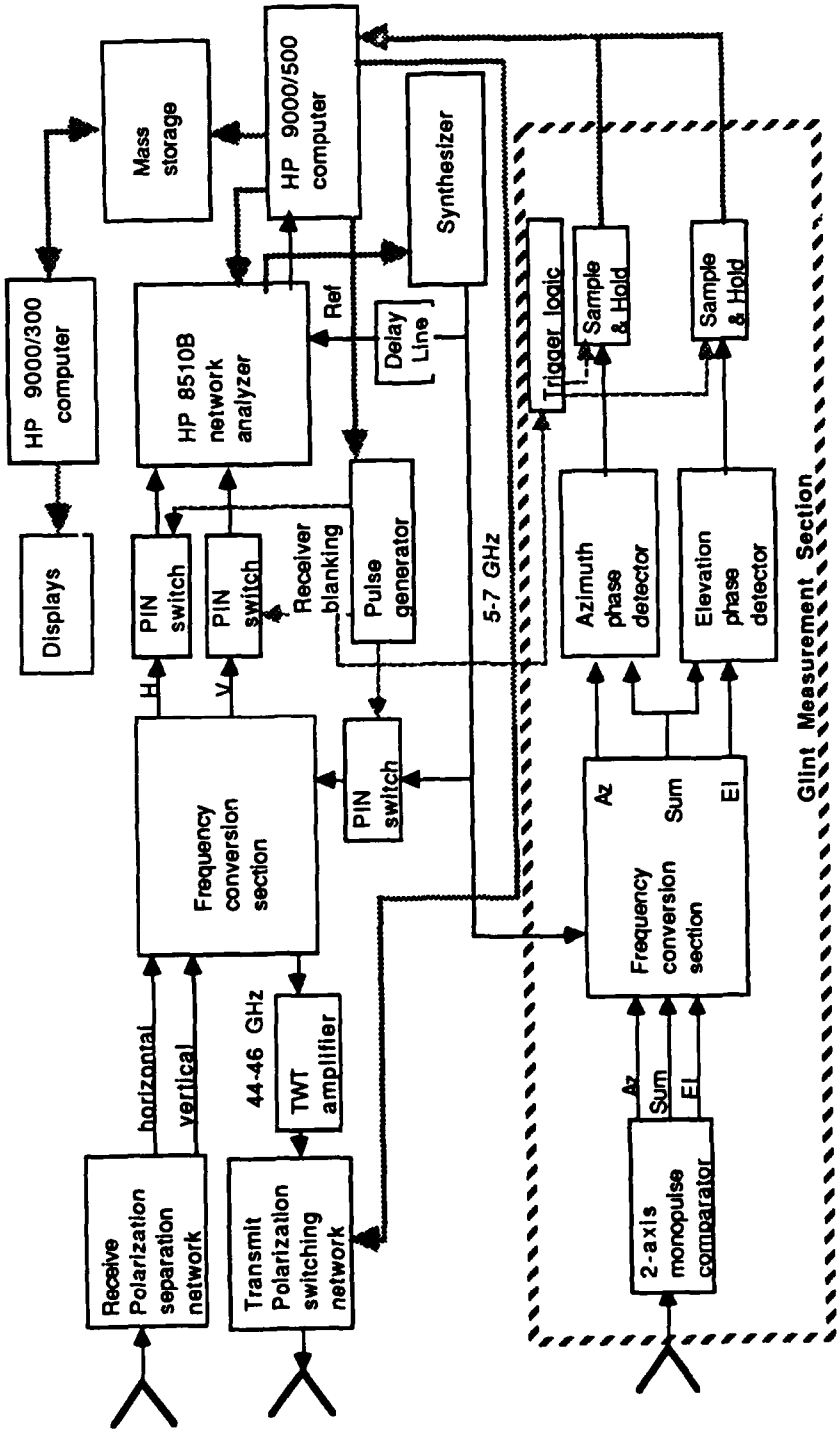

FIGURE 5. Block Diagram of 45-GHz Radar.

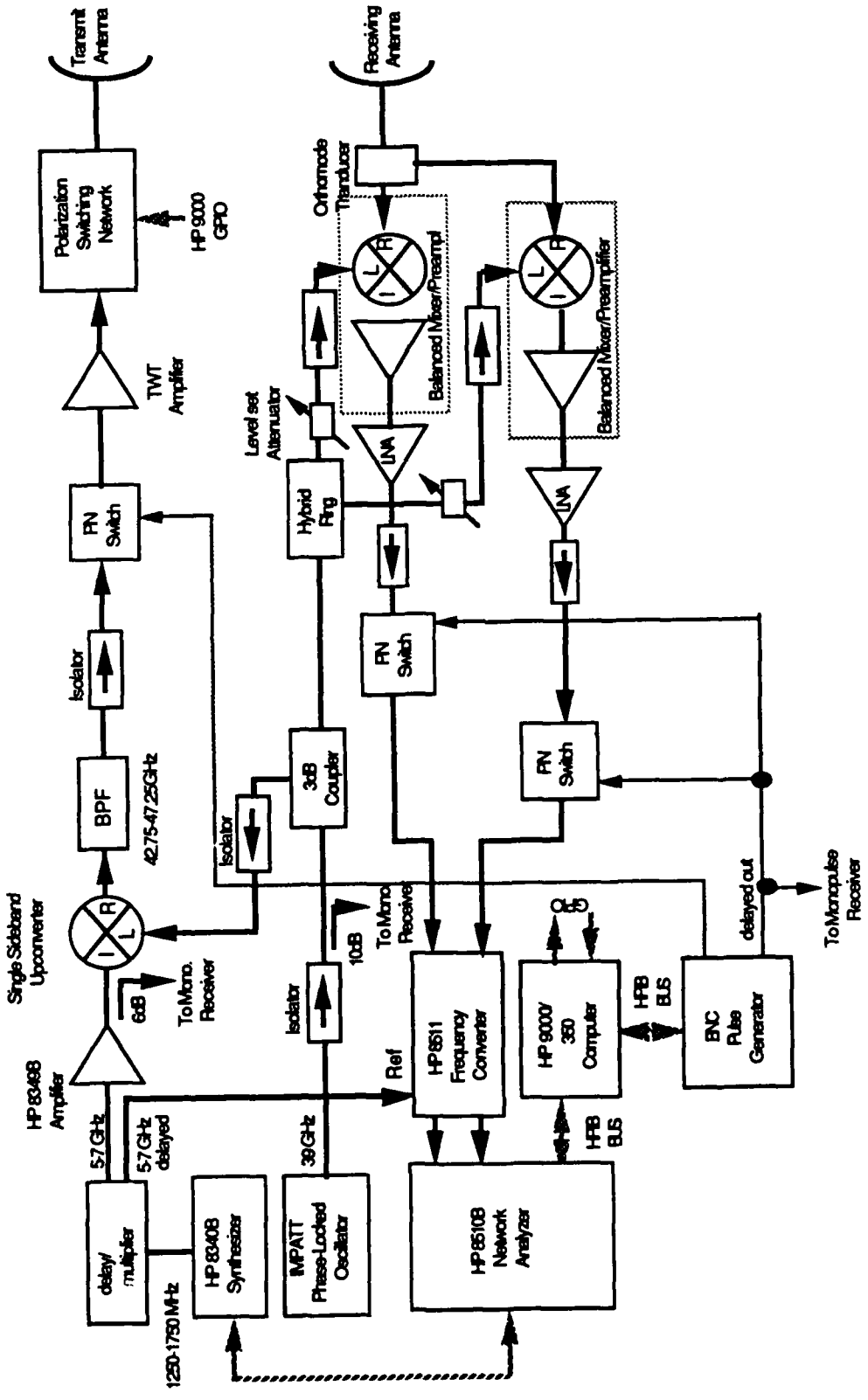

FIGURE 6. Transmit and RCS/ISAR Receiver Sections.

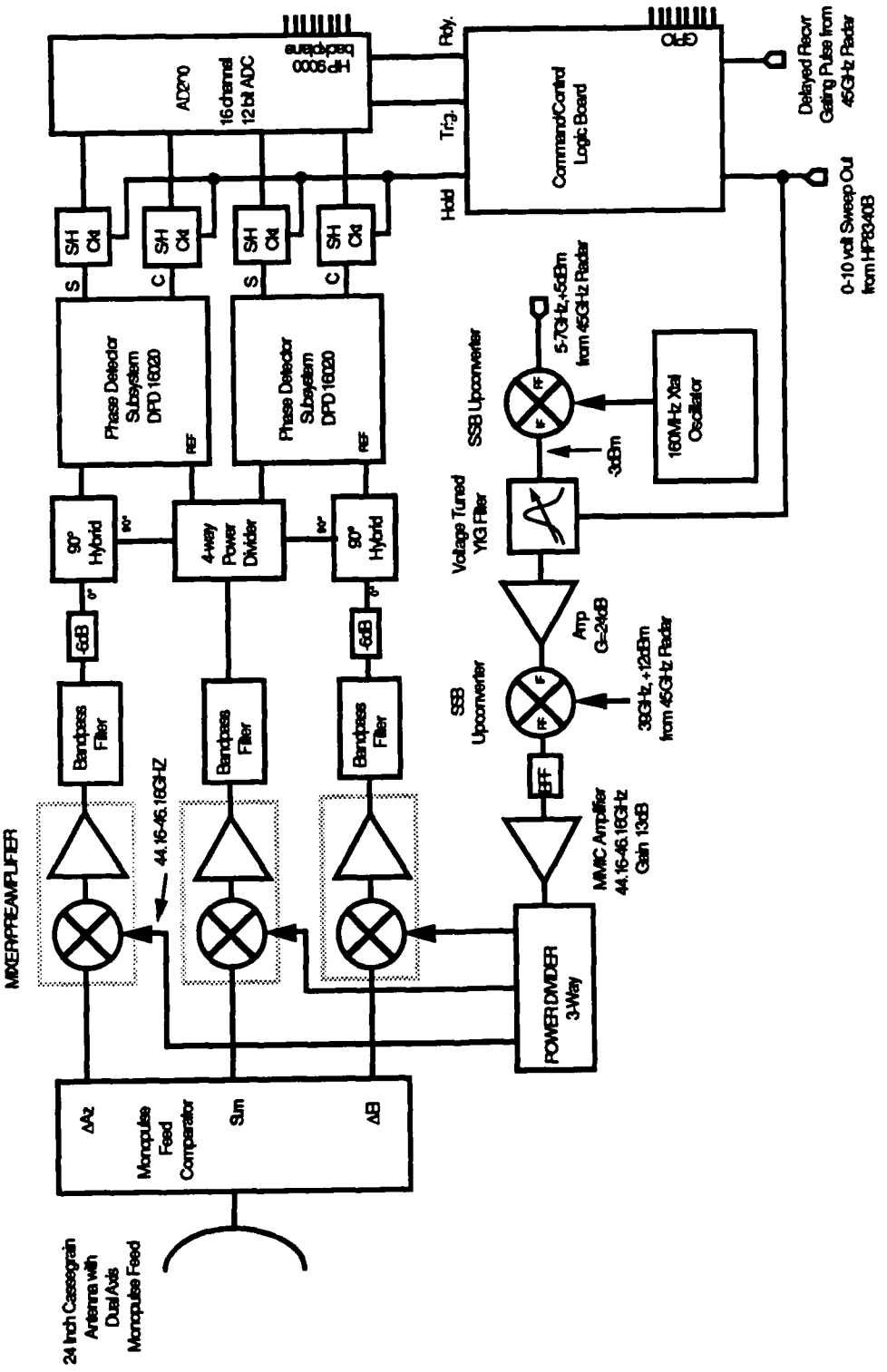

FIGURE 7. Monopulse Receiver Section.

3.2. TRANSMITTER

The synthesizer generates a stepped-frequency output over the interval from 1.25 to 1.75 GHz. The delay/multiplier (Figure 8) splits this output into two paths. The channel destined to be the reference signal passes through a 6.5-μs acoustic wave delay line, followed by two stages of frequency doubling to place the output in the 5- to 7-GHz band. The channel to be fed to the transmitter upconverter also has two stages of frequency doubling, but no delay.

The output of the transmitter upconverter (44 to 46 GHz), after bandpass filtering, is fed to a pin switch. This switch and the switches in the receiver paths are used to provide a hardware range gate to reduce direct coupling between the transmit and receive antennas. The output of the pin switch drives the TWT amplifier.

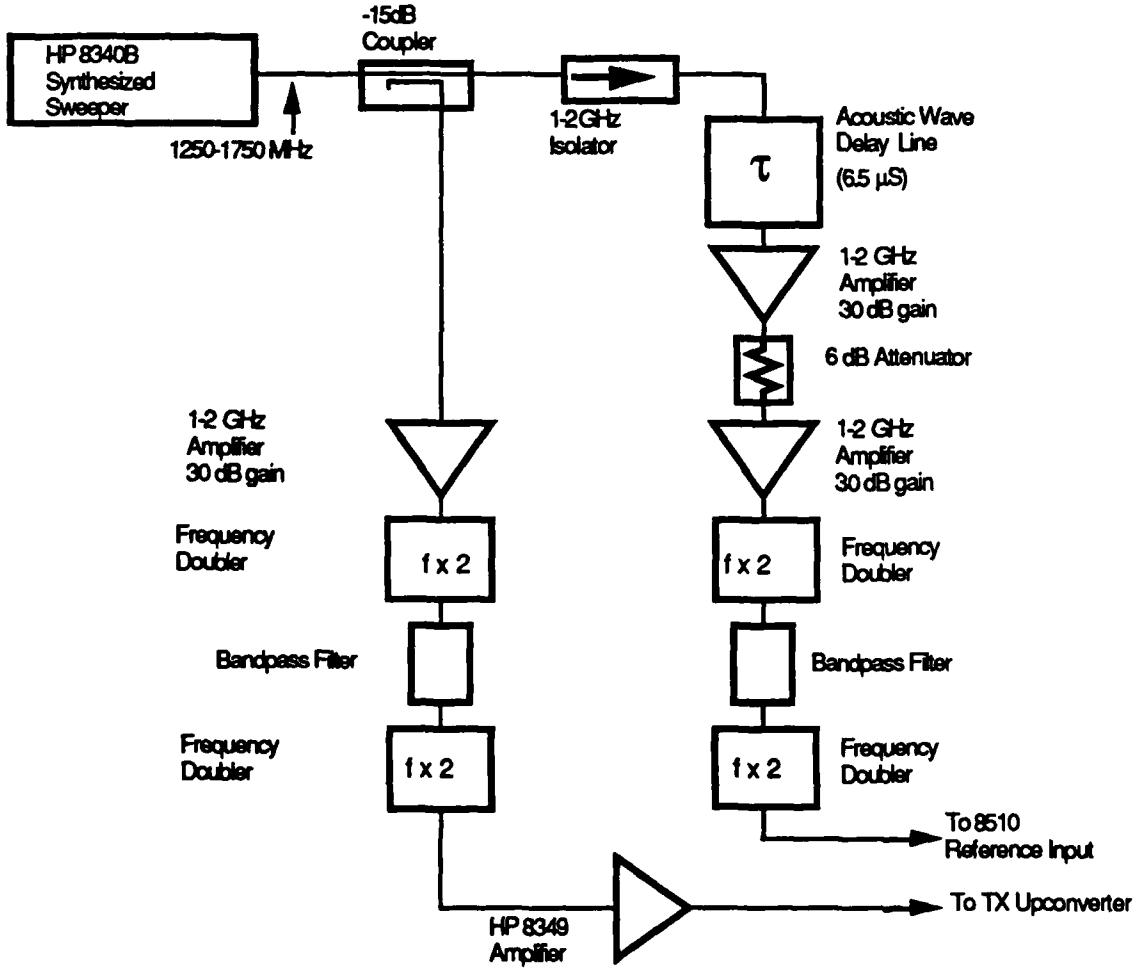

FIGURE 8. Delay/Multiplier Circuit.

The design challenge for the polarization switching network (Figure 9) is the high 30-W average power requirement. The diode window switches are reflective diode arrays (Reference 2) across the waveguide that are transparent in the off-state and reflective in the on-state. When in the on-state, the reflected power is absorbed in the load. One of the windows is always in the on-state and the other in the off-state; the desired polarization is set by the window in the off-state.

The transmit antenna is a 60-centimeter (cm) Cassegrain parabolic antenna. Figure 3 is a photograph of the antenna assembly, showing the transmitting antenna and the two receiving antennas. The antennas are mounted on a mechanical (nonmotorized) precision gimbal that permits accurate pointing of the 0.5-degree-beamwidth antennas.

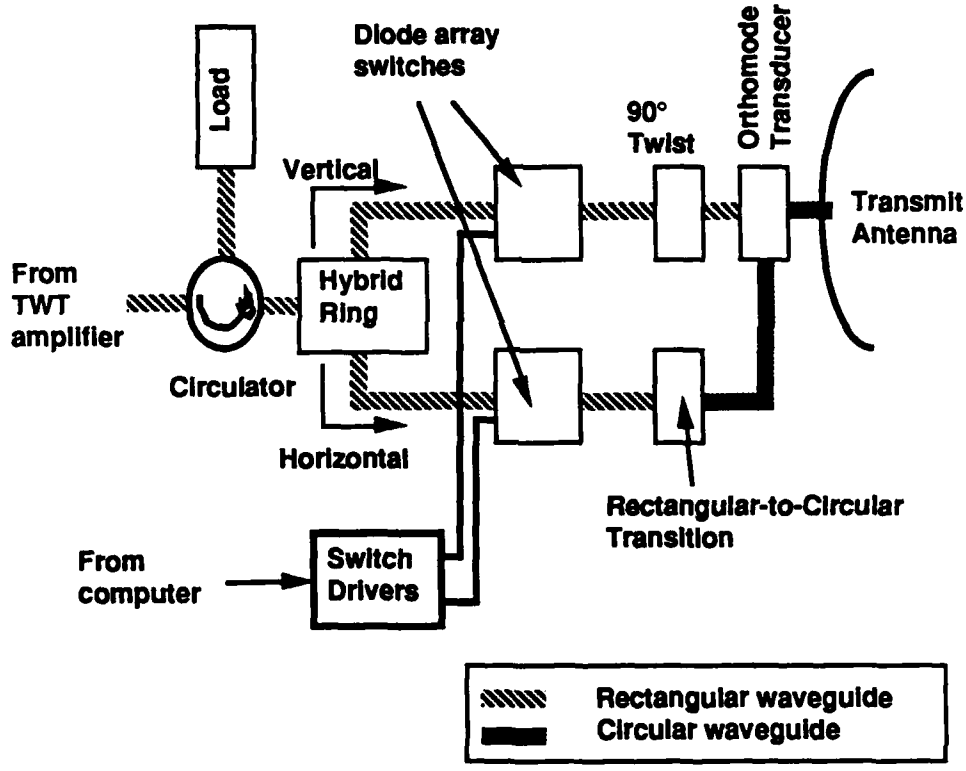

FIGURE 9. Transmitter Polarization Control Circuit.

3.3. ISAR RECEIVER

The receiving antenna is identical to the transmitting antenna and is mounted next to it. The linear vertical and horizontal components of the received signal are separated by an orthomode transducer and fed to balanced mixers whose local oscillator (LO) signals are provided by the 39-GHz impact avalanche and transit time (IMPATT) oscillator. The mixer outputs fall in the 5- to 7-GHz band needed for the HP-8510B. Following further amplification and filtering, the outputs are passed to pin

switches used for blanking the input to the HP-8510B receiver. These switches are driven from a digital delay pulse generator that provides a pulse delayed by 6.5 μs from the transmitter control pulse.

3.4. MONOPULSE RECEIVER

A 60-cm parabolic antenna with integral dual-axis monopulse comparator is the basis for the monopulse AOA receiver. The outputs of the sum beam-port and the azimuth and elevation difference beam-ports are downconverted using a reference signal of 44.16 to 46.16 GHz derived from the 39-GHz LO and the 5- to 7-GHz sweep output from the synthesizer. The yttrium-iron-garnet (YIG) voltage-tuned filter is required for filtering spurious outputs from the single-sideband upconverter. The mixer outputs thus are centered at an IF of 160 MHz.

After filtering, two phase detectors are used to develop outputs proportional to the sine and cosine of the phase between the sum and the difference channels. The 6-decibel attenuators in the azimuth and elevation difference channels are needed to balance the signal loss in the sum channel arising from the four-way power divider. The 90-degree hybrid produces an output signal with a phase given by $\phi = \tan^{-1}(\Delta/\Sigma)$, where Δ and Σ are the difference and sum beam signals, respectively. The phase detector sine and cosine channels then yield outputs given respectively (in volts) by

$$V_S = 2.5 \sin\phi = 2.5\,\Delta/(\Delta^2 + \Sigma^2)^{1/2} \tag{9}$$

and

$$V_C = 2.5 \cos\phi = 2.5\,\Sigma/(\Delta^2 + \Sigma^2)^{1/2}\ . \tag{10}$$

The theoretical and experimental variations of V_S and V_C measured during a calibration run are given in the section discussing radar calibration.

3.5. CONTROL AND DATA-PROCESSING COMPUTERS

As indicated in Figure 5, separate computers are used for radar control and data acquisition and for on-line data analysis. An HP-9000/500 computer controls all the functions and timing of the radar, including data acquisition. For maximizing the data-acquisition rate (as discussed in the next section), all of the error-processing and calibration functions that the HP-8510B is capable of carrying out internally are disabled (including the display), and the raw I and Q data are passed directly into the random access memory (RAM) of the HP-9000/500.

When taking full polarization data (all four combinations of vertical and horizontal transmit and receive polarizations), the 10-megabyte RAM capacity fills after 12 degrees of target rotation. At this point, the target is stopped and the data are stored to a hard disk. After storage, the target is then restarted and the measurements are continued.

While the data-acquisition continues, the data-analysis HP-9000/300 computer then accesses the hard disk and computes ISAR images for on-line analysis. These near-real-time images are essential for quality control and data assessment.

4. MAXIMIZING THE DATA-ACQUISITION RATE

A penalty paid for the flexibility of an HP-8510B-based radar is the relatively slow data-measurement rate; for the large L/λ ratios in the present case, a very large number of data points indeed must be taken, so that measurement time is an important consideration. To derive an equation for the maximum rotation rate of the target, note that the angular sampling interval $\delta\theta$ (the maximum change in target rotation angle between samples at the same frequency) is set by applying the Nyquist sampling criterion to the echo phase produced by a reflector at the edge of the target:

$$\delta\theta = \lambda/2L\xi \quad . \tag{11}$$

where ξ is the factor ($\xi \geq 1$) by which the angular sampling exceeds the Nyquist criterion. If N_p polarization states are required (each state requiring a separate sweep) and if each sweep requires T_S total time, then it follows that the rotation rate of the target is

$$\dot{\theta} = (10.8 \times 10^3)\, \lambda/2\pi L\xi N_p T_S \quad \text{(deg/min)} \quad . \tag{12}$$

In Figure 10 we plot $\dot{\theta}$ as a function of T_S. Note that very slow rotation rates are required. The total sweep time encompasses the synthesizer phase-lock time, the time for the sweep itself, a hand-off time for passing the data to a computer, and any internal processing time within the HP-8510B (such as error correction and display updating). We used the three following techniques to achieve the shortest possible T_S.

- *Ramp Mode.* In the stepped frequency mode of the HP-8510B, the synthesizer phase-locks to a commanded frequency at every frequency. Although this mode ensures high frequency accuracy, the length of time required for the synthesizer to lock causes the frequency dwell time per frequency to be 50 milliseconds (ms); for 201 frequency points, T_S would be at least 10 s, which is impractically long.

In the ramp mode, phase-lock occurs only for the first frequency, and then the frequency sweeps at a rate of about 0.2 ms per point. Some frequency accuracy is lost, but the total sweep time is much faster. The ramp mode is used in the radar; note, however, that for the 1000-meter radar-to-target range, the ramp mode requires the reference signal delay to prevent the echo from falling outside of the 10-kHz final bandwidth of the HP-8510B detection circuits. That is, for a frequency sweep rate f_r (Hz/s; note that $f_r \neq 1/T_S$, since T_S includes time periods when the frequency is not actually changing) and target range R, the instantaneous frequency of the return signal differs from the instantaneous frequency of the transmitted signal by $\Delta f = 2f_rR/c$. In the ramp mode, f_r = 25 GHz/s for a 1-GHz sweep interval and 201 points; hence, Δf = 42 kHz, which falls well outside the 10-kHz bandwidth. Delaying the reference avoids this problem.

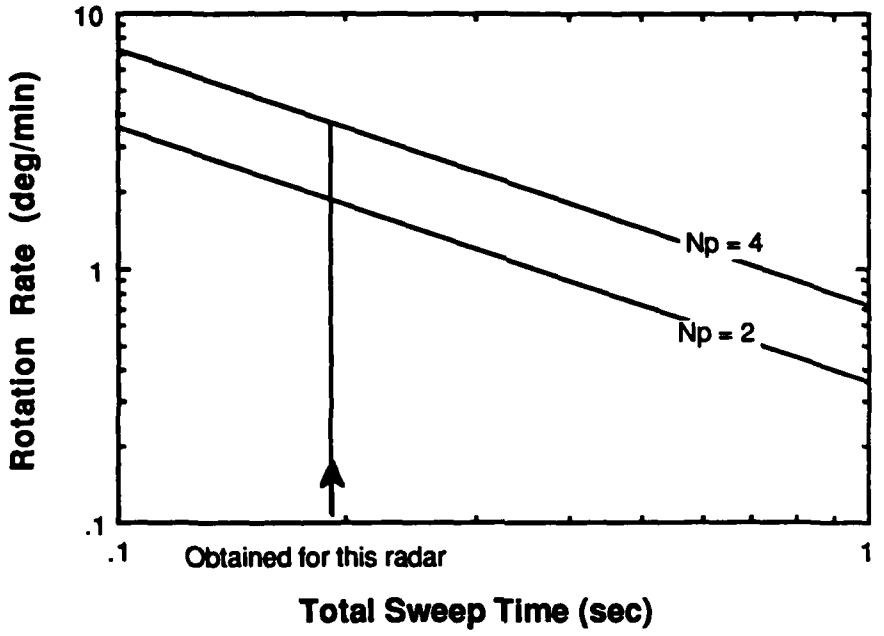

FIGURE 10. Total Sweep Time Versus Maximum Allowable Target Rotation Rate Obtained by Plotting Equation12 With L = 9 Meters and ξ = 1.0.

• *Bypassed Internal Error Correction in the HP-8510B.* We bypass the internal error correction routines in the HP-8510B and send the raw I and Q data directly to the controlling computer. The calibration and error corrections are applied after the test during data reduction.

• *Data Storage in RAM.* The raw I and Q data are stored in RAM during the target rotation; when the RAM is filled to capacity (after about 25 degrees of target rotation), the target is stopped and the data transferred to a hard disk.

Using these techniques, we are able to achieve a value of T_S = 0.19 s. By Figure 10, the rotation rate must be no greater than 3.8 deg/min for N_p = 4. In fact, we use a rotation rate of 2.1 deg/min to provide an aliasing margin of ξ = 1.8.

5. MINIMIZING TARGET SPURIOUS MOTION

Any motion of the target during the measurement that deviates from uniform rotation has the potential to introduce blurred scattering centers and false scattering centers due to aliasing. The Appendix analyzes a simple model of motion noise and demonstrates that the permissible amplitude of nonuniform rotation depends on the frequency components of the motion. The permissible amplitude-frequency product is

proportional to wavelength (Equation A-7), so that the problem is particularly severe for the relatively short 0.67-cm wavelength used here. Prior to the first measurements on the range, our uncertainty about what level of spurious motion to expect led us to consider a number of schemes to incorporate position-measuring sensors such as accelerometers and rate gyros in the targets and pylon. We rejected them because of the expense and problems of implementation.

It turns out that such techniques are not needed, as long as the measurements are carried out in dead calm wind conditions. The pylon is very rigid, so that free torsional motion and flexing are essentially nonexistent. The measurements must be carried out at night when wind speeds are lowest. In fact, throughout the principal measurement period in September 1989, the winds were dead calm. No artifacts or responses caused by spurious target rotation were observed.

6. RADAR CALIBRATION

6.1. COPOLARIZED RETURN

The dihedral diagrammed in Figure 11 (shown mounted in the 45-degree position) is used to calibrate the radar (Reference 3). Mounted in the vertical orientation (0-degree position), the dihedral has a calculable RCS from physical optics theory given by

$$\sigma_{VV} = \sigma_{HH} = 2\pi (ab)^2/\lambda^2 \quad , \tag{13}$$

where a is the length of the dihedral (102 cm), b is the maximum width of the face (35.8 cm), and λ is wavelength. For the calibration dihedral, this RCS is calculated as $\sigma_{VV} = \sigma_{HH} = 42.7$ decibels relative to one square meter (dBsm). The very large size of this dihedral compared to a wavelength ($a/\lambda \approx 152$) ensures that the physical optics limit required by Equation 13 is satisfied. The edges of the dihedral were beveled at an angle of 15 degrees to produce a knife-edge and hence minimize the return from edge diffraction.

6.2. CROSS-POLARIZED RETURN

Following a measurement of the dihedral in the 0-degree position, the dihedral was mounted at an angle of 45 degrees. In this position, the dihedral (in the physical optics limit) produces an RCS in the cross-polarization channel that also is given by Equation 13 and produces no return in the copolarized channel. That is, the dihedral functions as an ideal polarization transformer.

To avoid possible errors arising from receiver saturation, these calibration RCS values should be somewhat smaller. However, this size dihedral was the smallest that would effectively shadow the rotator (as shown in Figure 11).

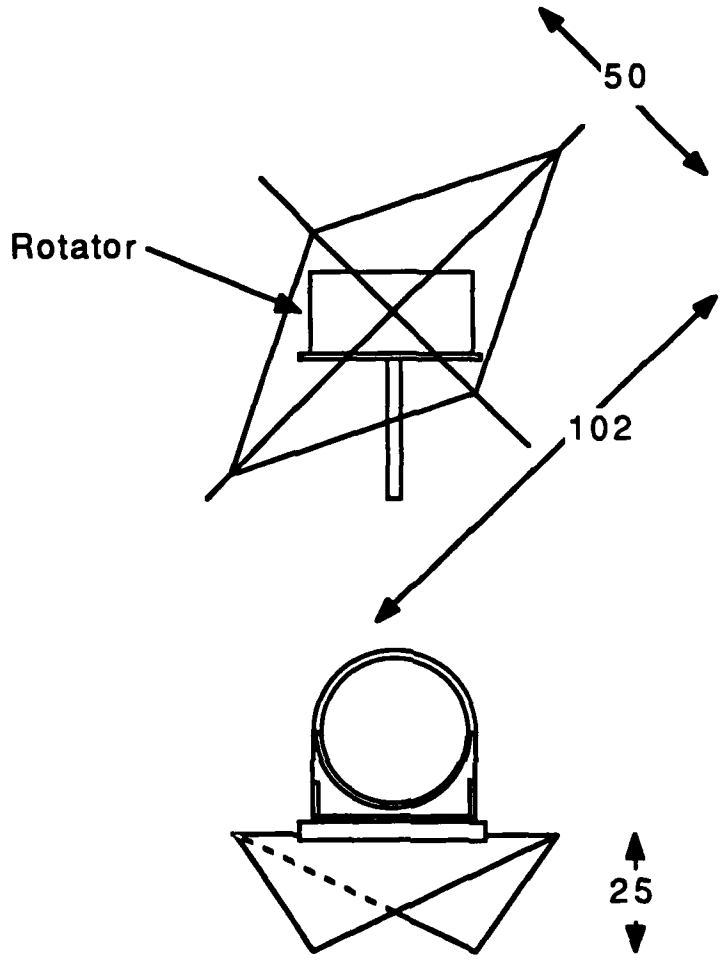

FIGURE 11. Calibration Dihedral as Mounted on the Rotator in the 45-Degree Position. The 0-degree position places the trough of the dihedral in a vertical orientation. Dimensions are in centimeters.

6.3. MONOPULSE AOA CALIBRATION

Ideally, it would be desirable to calibrate the monopulse channel by moving a point reflector throughout the target zone. However, a variety of mechanical, electrical, and rotator-shielding problems make this approach completely impractical. Therefore, to calibrate the monopulse channel, the dihedral was mounted in the 0-degree position and the radar antenna gimbal was manually scanned through the target zone in steps of 0.14 degree in the azimuth and elevation planes. The outputs of the monopulse channel phase detectors were recorded as a function of the antenna gimbal position. Moving the antennas in this manner is equivalent to moving a point target in the target zone itself only to the extent that the clutter observed by the radar does not change as the antenna gimbal is scanned.

Figure 12 is a plot of a typical azimuth calibration curve. For comparison, theoretical curves are also shown that were calculated using the measured monopulse sum and difference antenna patterns supplied by the manufacturer. The calibration curves agree approximately with the theory.

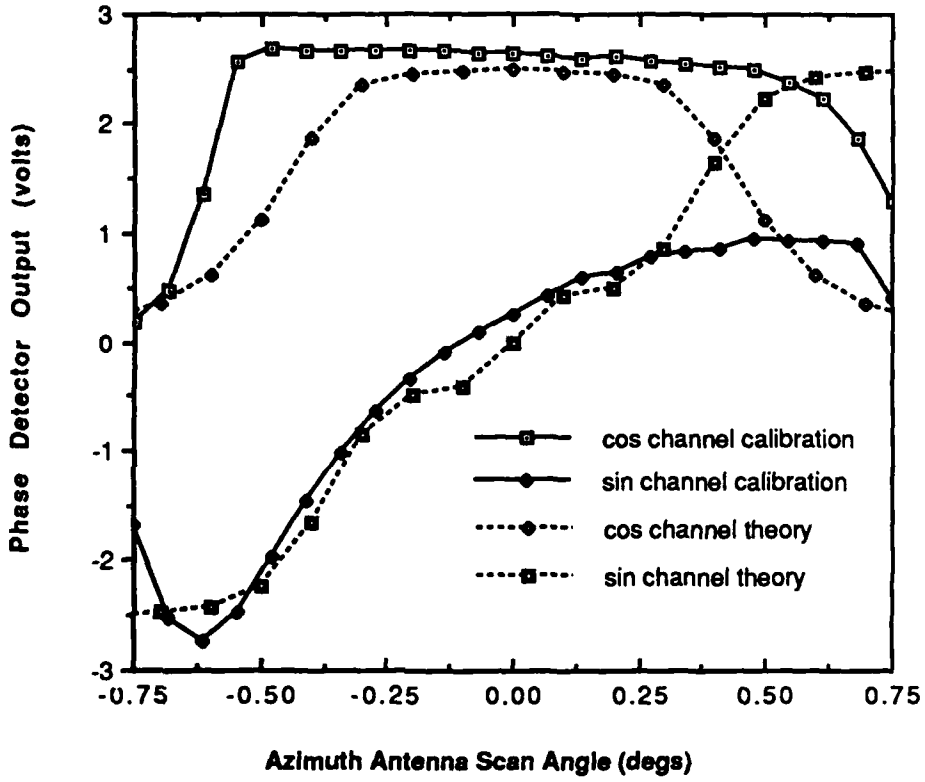

FIGURE 12. Output of the Monopulse Phase Detectors as the Antenna Gimbal Is Scanned Through the Target Zone With a Dihedral Calibration Target.

7. SAMPLE MEASUREMENTS

Figure 13 is an example of an AOA measurement taken on a 1:60 scale model of a medium-sized bomber aircraft. The AOA was derived from the sine channel output of the phase detector (as given by Equation 9). The approximate length of the model is 60 cm. The trace shows "bright spot wander" and large excursions in the apparent target center at broadside that are typical of glint data. The trace is offset from the boresight

position of the antenna, because the monopulse antenna was not pointed directly at the target center. This measurement was made at a radar-to-target range of 130 meters.

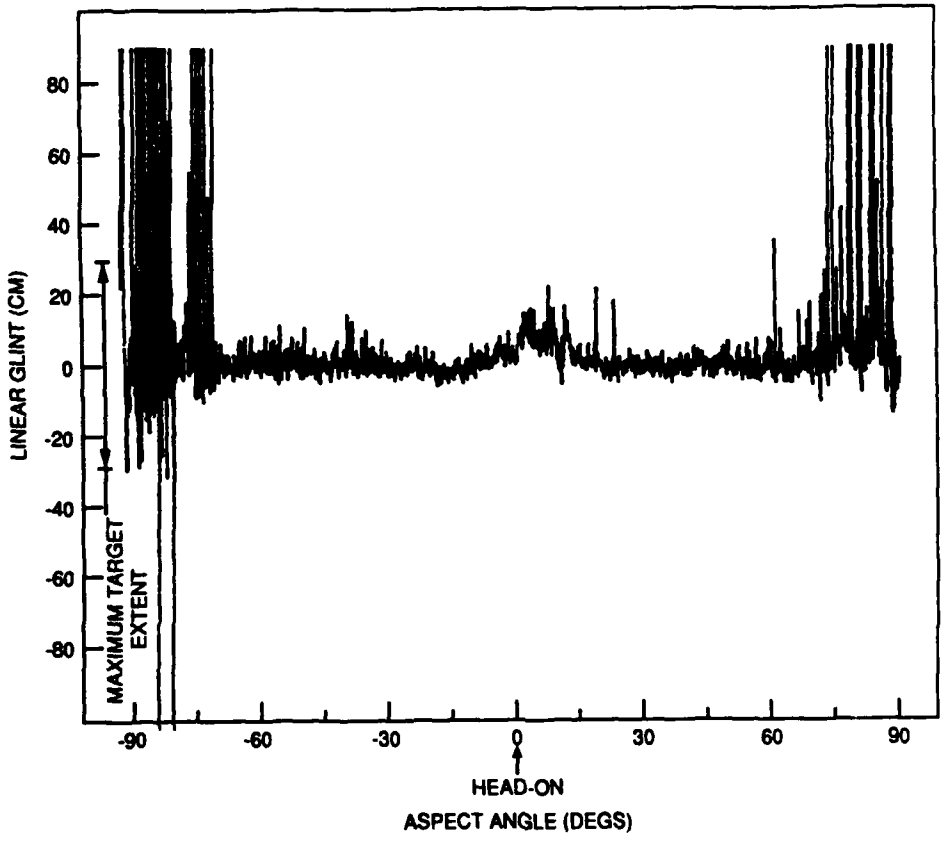

FIGURE 13. Variation of the Apparent Center of Scattering of a Model Aircraft Target as the Target Is Rotated.

Figure 14 gives an example of an ISAR image of an 8-meter one-fifth-scale aircraft target. No spurious responses or image blurring are observed in the images attributable to target/pylon vibration, wind-induced vibrations, an insufficient sampling rate, or similar experimental deficiencies. We had been concerned that the combination of a subcentimeter wavelength and the out-of-doors operation might make sharp ISAR images unobtainable in spite of our best efforts.

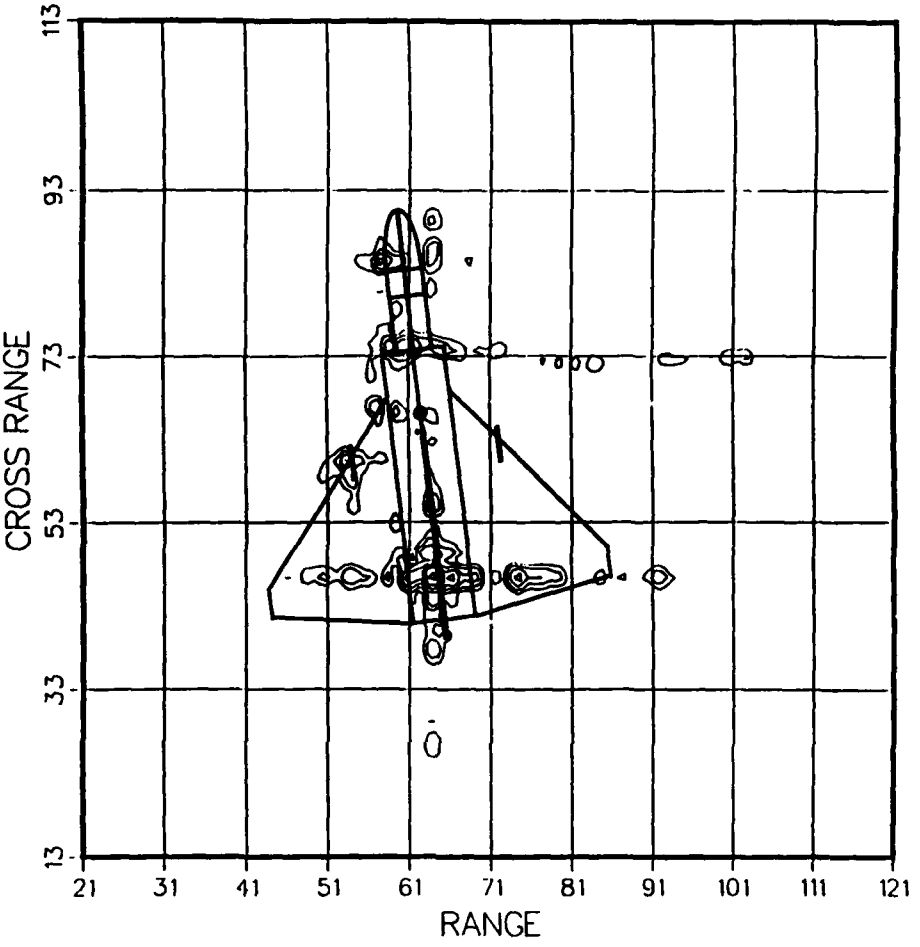

FIGURE 14. ISAR Contour Plots of a Model Aircraft Target. The radar is located at the left, viewing the target in near-broadside aspect. The numbers of the abscissa and ordinate are the indices of the two-dimensional Fourier transform used to form the image. B = 1.0 GHz; $\Delta\theta$ = 1.6 degrees.

8. CONCLUSIONS

A 45-gigahertz radar has been developed that yields full-polarization inverse synthetic aperture radar images and instantaneous angle-of-arrival measurements for angular scintillation studies. The system is portable and self-contained. Measurements have been successfully made on large scale-model targets at a range of 1000 meters.

Appendix

BLURRING OF THE IMAGE CAUSED BY NONUNIFORM ROTATIONAL MOTION

The purpose of this Appendix is to calculate the amplitude and frequency of *nonuniform* target azimuthal rotation that can lead to target blurring. We use the following simple model. Consider a target that is rotating about the z-axis (Figure 1 of main text) according to

$$\theta(t) = \Omega t + \theta_n \sin \omega_n t \ , \qquad \text{(A-1)}$$

where the first term is the desired uniform rotation at a rate Ω and the second term is "noise" with an amplitude θ_n and frequency ω_n caused by backlash, wind, etc. Near broadside, the downrange displacement for a point on the target located a distance r from the center of rotation is

$$y = \rho\theta = \rho\Omega t + \rho\theta_n \sin \omega_n t \ . \qquad \text{A-2)}$$

For an interval between samples (at a given frequency) of Δt, the downrange change in displacement is given by

$$\Delta y = \rho\Omega \, \Delta t + \rho\theta_n\omega_n \cos \omega_n t \, \Delta t \ . \qquad \text{(A-3)}$$

The performance limits for image formation occur when Δy is a maximum, which occurs when $\omega_n t = (n - 1)\pi$ (n any integer). In this case,

$$\Delta y = (\rho\Omega + \rho\theta_n\omega_n) \, \Delta t \ . \qquad \text{(A-4)}$$

Recovery of the phase variation requires that $\Delta y \le \lambda/2$, which leads to the condition

$$\theta_n\omega_n \le (\lambda/2\rho\Delta t) - \Omega \ . \qquad \text{(A-5)}$$

The rotation rate Ω is set by the same Nyquist criterion discussed in regard to Equation 10 in main text; this equation leads to

$$\Omega = \delta\theta/\Delta t = \lambda/2L\xi\Delta t \ . \qquad \text{(A-6)}$$

Hence, the condition on the frequency and amplitude of the noise term in Equation A-5 becomes

$$\theta_n\omega_n \le (\lambda/2\Delta t)[1/\rho - 1/L\xi] \qquad (0 \le \rho \le L/2) \ . \qquad \text{(A-7)}$$

A plot of the equality in Equation A-7 is given in Figure A-1 for the parameters appropriate to the 45-gigahertz radar for two different values of ρ. These curves are approximate boundaries between a blurred image (at a given value of ρ) and an unblurred image. The upper right-hand portion of the plot corresponds to conditions that blur the image; the lower left-hand portion corresponds to conditions that do not.

At the edge of the target (ρ = 450 cm), for example, the nonuniform motion at a frequency of 0.1 hertz must have an angular amplitude less than about 0.08 degree to prevent blurring.

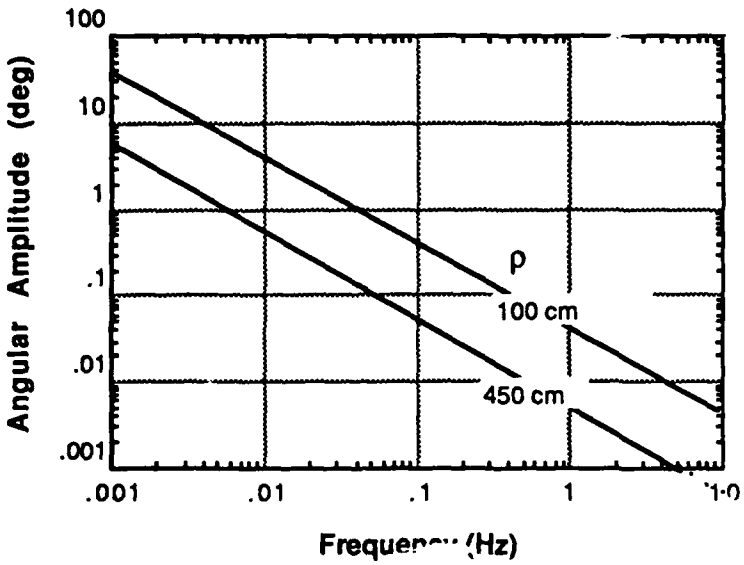

FIGURE A-1. At a Given Distance ρ From the Center of Rotation, a Plot of the Boundary Between the Combination of Nonuniform Angular Rotation Amplitude and Rotation Frequency That Permits Sufficient Sampling of the Phase Variation (Lower Left) and Undersampling (Upper Right). Undersampling will produce blurring and/or image aliases.

INITIAL DISTRIBUTION

8 Naval Air Systems Command
- AIR-5004 (2)
- AIR-5401C (1)
- AIR-93 (1)
- AIR-932 (1)
- AIR-932G (1)
- PMA-208 (1)
- PMA-259 (1)

6 Chief of Naval Operations
- OP-35 (1)
- OP-50 (1)
- OP-954 (1)
- OP-955 (1)
- OP-98 (1)
- OP-987 (1)

4 Chief of Naval Research
- OCNR-20 (1)
- OCNR-21 (1)
- OCNR-213, D. Siegel (1)
- OCNR-214, J. Hall (1)

3 Naval Sea Systems Command
- PMS-422 (1)
- Technical Library (2)

1 Commander in Chief, U. S. Pacific Fleet, Pearl Harbor (Code 325)
1 Commander, Third Fleet, San Francisco
1 Commander, Seventh Fleet, San Francisco
2 Naval Academy, Annapolis (Director of Research)
1 Naval Air Development Center, Warminster (Code 50B, Kessler)
1 Naval Ocean Systems Center, San Diego (D. Wehner)
4 Naval Research Laboratory
- Code 5300, Olin (1)
- Code 5307, Jedrey (1)
- Code 5340, Cantrell (1)
- E. Althouse (1)

1 Naval Surface Warfare Center, Dahlgren (Code F41, Morrissett)
1 Naval War College, Newport
2 Pacific Missile Test Center, Point Mugu
- Code 1052, P. Yu (1)
- Dr. D. L. Mensa (1)

2 Army Missile Command, Redstone Arsenal
- Code AMCLD (1)
- Code AMSMI-RD-AS (1)

1 Air Force Intelligence Agency, Bolling Air Force Base (AFIA/INTAW, Maj. R. Esaw)
2 Air Force Munitions Systems Division, Eglin Air Force Base
- AFATL/AS (1)
- AFATL/CCN (1)

2 Defense Technical Information Center, Alexandria
1 Aerospace Corporation, El Segundo, CA (R. Dybdal)
1 Denmar, Incorporated, Chandler, AZ (S. Brumley)
1 Electromagnetic Sciences, Norcross, GA (G. Hickman)
1 Flam and Russell, Incorporated, Horsham, PA (Dr. L. Burgess)
1 Georgia Institute of Technology, School of Electrical Engineering, Atlanta, GA (Dr. E. B. Joy)
2 Hewlett Packard, Santa Rosa, CA
- J. W. Boyles (1)
- J. Swanstrom (1)

1 Hudson Institute, Incorporated, Center for Naval Analyses, Alexandria, VA (Technical Library)
1 Hughes Aircraft Company, Los Angeles, CA (A. R. Lamb)
1 Hughes Aircraft Company, Torrance, CA (J. A. Paul)
1 IIT Research Institute, GACIAC, Chicago, IL (Dr. R. J. Heaston)
1 Information Systems and Research, Incorporated, Fairfax, VA (Dr. J. C. Davis)
1 Lockheed Advanced Development Company, Burbank, CA (R. R. Taron)
1 Ohio State University, ElectroScience Lab, Columbus, OH
  Dr. W. D. Burnside (1)
  Dr. E. K. Walton (1)
1 Scientific-Atlanta, Incorporated, Norcross, GA (M. L. Wolfenbarger)
4 The Johns Hopkins University, Applied Physics Laboratory, Laurel, MD
  Code BBE, L. Weckesser (1)
  Code BBP, J. Kiersey (1)
  Code BFD, E. Marley (1)
  Code F1, R. LaFever (1)
1 TRW Mead, San Diego, CA (Dr. C. H. Walter)
1 University of Houston, Department of Electrical Engineering, Houston, TX (Dr. J. T. Williams)